Synchrotron x-ray study of a low roughness and high efficiency K_2CsSb photocathode during film growth

2017 J. Phys. D: Appl. Phys. 50 205303

(http://iopscience.iop.org/0022-3727/50/20/205303)

IOP Publishing Journal of Physics D: Applied Physics
J. Phys. D: Appl. Phys. **50** (2017) 205303 (8pp) https://doi.org/10.1088/1361-6463/aa6882

Synchrotron x-ray study of a low roughness and high efficiency K_2CsSb photocathode during film growth

Junqi Xie[1,6], Marcel Demarteau[1], Robert Wagner[1], Susanne Schubert[2,3], Mengjia Gaowei[2], Klaus Attenkofer[2], John Walsh[2], John Smedley[2,6], Jared Wong[3], Jun Feng[3], Howard Padmore[3], Miguel Ruiz-Oses[4,5], Zihao Ding[4], Xue Liang[4], Erik Muller[4] and Ilan Ben-Zvi[2,4]

[1] Argonne National Laboratory, 9700 S. Cass Ave., Argonne, IL 60439, United States of America
[2] Brookhaven National Laboratory, 2 Center St., Upton, NY 11973, United States of America
[3] Lawrence Berkeley National Laboratory, 1 Cyclotron Rd., Berkeley, CA 94720, United States of America
[4] Stony Brook University, Stony Brook, NY 11794, United States of America
[5] Present address: Fritz Haber Institute, Faradayweg 4-6, Berlin 14195, Germany

E-mail: jxie@anl.gov and smedley@bnl.gov

Received 31 May 2016, revised 15 February 2017
Accepted for publication 22 March 2017
Published 24 April 2017

Abstract

Reduction of roughness to the nm level is critical of achieving the ultimate performance from photocathodes used in high gradient fields. The thrust of this paper is to explore the evolution of roughness during sequential growth, and to show that deposition of multilayer structures consisting of very thin reacted layers results in an nm level smooth photocathode. Synchrotron x-ray methods were applied to study the multi-step growth process of a high efficiency K_2CsSb photocathode. A transition point of the Sb film grown on Si was observed at the film thickness of ~40 Å with the substrate temperature at 100 °C and the growth rate at 0.1 Å s^{-1}. The final K_2CsSb photocathode exhibits a thickness of around five times that of the total deposited Sb film regardless of how the Sb film was grown. The film surface roughening process occurs first at the step when K diffuses into the crystalline Sb. The photocathode obtained from the multi-step growth exhibits roughness in an order of magnitude lower than the normal sequential process. X-ray diffraction measurements show that the material goes through two structural changes of the crystalline phase during formation, from crystalline Sb to K_3Sb and finally to K_2CsSb.

Keywords: bialkali antimonide photocathode, grazing incidence small angle x-ray scattering, x-ray reflectivity, x-ray diffraction, thickness, roughness, critical angle

(Some figures may appear in colour only in the online journal)

1. Introduction

Over the last few decades, many kinds of photoemissive materials have been used as photocathodes to generate free electrons in practical applications. For example, robust metal photocathodes are used in accelerator-based light sources [1–3] and low work function compound photocathodes are used in photomultiplier tubes [4–6]. Photocathodes for electron accelerator applications such as energy recovery linacs (ERL) and free electron lasers (FEL) must operate with a very low transverse energy. However, electrons photo-excited from the cathode must be accelerated to relativistic velocities in the smallest possible distances to avoid the deleterious effects of space charge [7]. This requires that the photocathode should operate in a very high longitudinal electric field, up to 10^8 V m^{-1}, typically provided by a high power resonant radio frequency

[6] Authors to whom any correspondence should be addressed.

(RF) cavity. However, roughness, which will induce local tilts into the surface, results in transverse acceleration of the electrons and increase in their average energy. At gradients of 20 MV m^{-1} for example, nm perpendicular height change (with domain sizes of five times the height) causes a kT-equivalent increase in the transverse emittance [8]. This suggests that the roughness of the photocathode must be reduced to sub nm levels to achieve the highest beam brightness. Newly proposed high brightness light sources have demanded electron beams with very low transverse emittance as well as long-life time and high quantum efficiency (QE) photocathodes in the visible light region [9, 10].

Among various photocathode materials, alkali antimonides, such as K_3Sb, Cs_3Sb, K_2CsSb and Na_2KSb, have great promise in the application of future light sources because of their high QE, fast response time and low thermal emittance [11–15]. Especially, the bialkali photocathode, K_2CsSb, exhibits QE over 5% in the green light range, several orders of magnitude higher than that of a metal photocathode (typical QE ~ 10^{-5}) [1, 13]. Test results of K_2CsSb photocathodes under laser illumination show a low emittance of 0.37 μm mm^{-1} rms^{-1} at 543 nm and a reasonable life time of over 20 h even with relatively high residual water contamination [14].

The K_2CsSb bialkali photocathode was first reported in the 1960s by Sommer [16] and much effort has been devoted to investigate its characteristics since then. The photoemission, photoconductivity and optical absorption of K_2CsSb as a function of wavelength were subsequently measured, and the bandgap energy and electron affinity were determined [17]. Chemical analysis of the photocathode indicated its stoichiometric formula of K_2CsSb, which was confirmed by x-ray diffraction (XRD) studies [18]. The electronic structure of K_2CsSb was also calculated using the localized spherical wave method (LSW) to explain its optical properties [19]. However, the studies of the electro-optical properties and chemical composition did not lead to a major improvement in the fabrication of K_2CsSb photocathodes with high quantum yield. Only very few results were reported on bialkali photocathode development by commercial manufacturers [20, 21]. These improvements were mainly obtained by structuring the substrate surface and paying attention to the details of the growth. Furthermore, a survey of literature shows that there is no study on the photocathode surface morphology except a reported value of ~25 nm measured from a photocathode through traditional sequential growth [22]. Due to the fact that alkali antimonides are sensitive to air and water, the K_2CsSb photocathode is always deposited on the inner surface of a sealed vacuum envelope in industrial photomultipliers. This configuration makes it difficult to directly characterize the K_2CsSb photocathode using *ex situ* thin film characterization tools. *In situ* characterization techniques are critical to investigate its thickness, surface morphology, structure, grain size and growth details.

Synchrotron x-ray measurements are well established and widely used, both *in situ* and *ex situ*, as rapid, simple, noncontact and nondestructive thin film characterization methods. These x-ray techniques utilize differing geometries and use different x-ray beam characteristics. For example, grazing incidence small angle x-ray scattering (GISAXS) records the 2D x-ray scattering pattern of the incident beam near the critical angle to probe the film surface morphology [23]; x-ray reflectivity (XRR) records the specular x-ray reflection intensity curve from a grazing incident x-ray beam to determine film thickness, electron density, as well as surface and interface roughness [24]; and XRD records the diffracted beam from a wide angle x-ray beam to determine film structure and grain size [25]. We have developed tools combining the GISAXS, XRR and XRD techniques to *in situ* study the growth process of bialkali antimonide photocathodes, to understand the formation of the photocathode and to improve the QE and surface roughness of the photocathode by optimization of the deposition process.

In this work, we deposited high QE K_2CsSb photocathodes on Si (1 0 0) substrates by alternately introducing antimony (Sb), potassium (K) and cesium (Cs) vapors in multi steps consisting of very thin reacted layers with the attempt to reduce the photocathode surface roughness. *In situ* real time synchrotron x-ray scattering, reflection and diffraction measurements were performed to explore the evolution of thickness, roughness, density and structure during the photocathode film growth.

2. Materials and methods

2.1. Thin film growth

The thin film growth was performed in a custom-built ultra-high vacuum chamber equipped with several scroll and turbo molecular pumps to ensure a base pressure in the low 10^{-10} Torr level. After a full bake out at 200 °C, the partial pressures of reactive gases (H_2O, O_2) were well below 5×10^{-11} torr, confirmed by a residual gas analyzer. Each 1 cm × 2 cm Si (1 0 0) substrate was first degreased in acetone and isopropanol alcohol for 30 min, and then etched in diluted aqueous hydrofluoric acid (HF) solution for 5 min to remove the native oxide layer. After HF treatment, the substrate was rinsed with deionized water, dried under a steam of high purity nitrogen and immediately inserted into the growth chamber through a load lock. Prior to growth, the substrate was heated at 500 °C under high vacuum for further surface cleaning treatment until the base pressure of the chamber was restored. The K_2CsSb photocathode film was produced by alternately introducing Sb, K and Cs vapors. Sb was generated by thermal evaporation of an Sb–Pt alloy, using resistive heating of a bead of material on beryllium/tungsten wire. This ensured that Sb was produced as monomers, rather than as small clusters normally produced from elemental Sb [26]. Alkali metals were produced from dispensers (purchased from Alvatec Alkali Vacuum Technologies GmbH, Austria) containing intermetallic bismuth-alkali compounds. These solid sources were mounted directly facing the substrate at a distance of 7.5 cm. During photocathode growth, the substrate was kept at ~125 °C; the individual vapor deposition thicknesses, growth rates and the photocathode photoresponses were monitored with a pre-calibrated quartz crystal microbalance (QCM) and an electrometer. First, Sb was evaporated onto Si (1 0 0) at a growth rate of 0.2 Å s^{-1}. The Sb film was then exposed to K vapor until the photocurrent

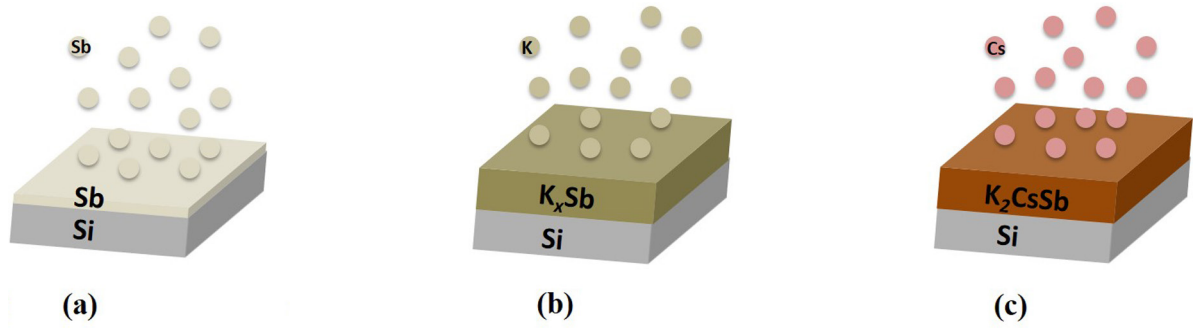

Figure 1. Schematic diagram shows the diffusion process of the K_2CsSb photocathode: (a) Sb thin film deposition; (b) K diffusion forming a K_xSb compound; and (c) Cs diffusion forming a K_2CsSb photocathode.

reached a plateau. Subsequently, the film was exposed to Cs vapor, forming the K_2CsSb photocathode. The Cs exposure was terminated when the photocurrent reached another plateau. Specifically, the processing of the K_2CsSb photocathode may be expressed as the following empirical diagram of equation (1) and schematic diagram of figure 1:

$$\mathrm{Sb} + \mathrm{K} \xrightarrow{\sim 125\ ^\circ\mathrm{C}} \mathrm{K}_x\mathrm{Sb} + \mathrm{Cs} \xrightarrow{\sim 125\ ^\circ\mathrm{C}} \mathrm{K}_2\mathrm{CsSb}. \qquad (1)$$

This process was repeated in the current work to maximize the photocathode photoresponse. The photoresponse could be improved with a second layer growth, but a third layer did not yield a further increase.

2.2. QE measurement

During the thin film deposition, photoresponse was recorded to monitor the film growth process and to determine the completion of film deposition. A continuous incident laser with 532 nm wavelength was positioned to generate a laser spot on the surface of the photocathode. The laser power (P_0) was measured with a silicon power meter, and the laser spot is around 1 mm diameter. A metal dynode was placed in front of the photocathode surface with a distance of 1 cm. By applying a negative bias of -20 V, the photoresponse current (I_{ph}) was measured with a Keithley 6517B electrometer. The QE was then calculated with the following equation:

$$\mathrm{QE} = \frac{hcI_{\mathrm{ph}}}{e\lambda P_0} = \frac{1240 I_{\mathrm{ph}}(\mathrm{A})}{\lambda(\mathrm{nm}) P_0(\mathrm{W})}$$

where h is the Planck constant, c is the speed of light, e is the elementary charge and λ is the light wavelength.

2.3. Synchrotron x-ray measurements

The x-ray scattering, reflection and diffraction measurements were performed at the national synchrotron light source (NSLS) X21 station. Synchrotron x-ray beam with 10 keV energy and 2×10^{12} photons s^{-1} flux was employed to study the thin film growth. The x-ray probe beam was allowed to enter and exit the growth chamber through two beryllium windows, and the x-ray data were recorded by two Pilatus 100 K silicon diode array area detectors with a pixel size of 172 μm $\times$ 172 μm (487 $\times$ 195 pixels) and a readout time of less than 2.7 ms. A schematic diagram of the *in situ* real time x-ray measurement setup is shown in figure 2. During film growth, the grazing incidence angle α_i was fixed at 1.8°. X-ray scattering and diffraction patterns were recorded by the area detectors with an exposure time of 20 s/frame. After the completion of each vapor exposure, *in situ* XRR and XRD scans were taken in a $\theta - 2\theta$ geometry, from $2\theta = 0°$ to $2\theta = 8°$ at a step size of 0.02°/frame and from $2\theta = 9°$ to $2\theta = 35°$ at a step size of 1°/frame, respectively. XRR intensity parameters were extracted from the raw frame images and fitted following Parratt's recursion [27] to simulate the film thickness, electron density and surface roughness. XRD patterns were also extracted and compared with standard data sets to determine the film structure and textures.

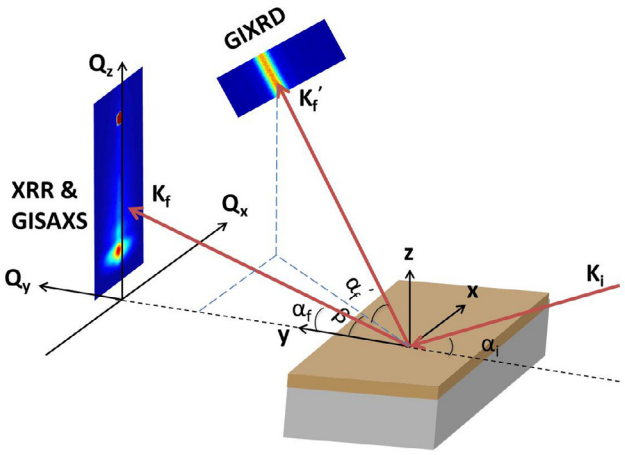

Figure 2. Schematic diagram of the *in situ* real time x-ray measurement setup.

3. Results and discussion

3.1. Growth of an antimony film

The basic process of alkali antimonide photocathode fabrication consists of two steps: (1) deposition of an initial Sb film on the substrate, and (2) sequential diffusion of alkali vapors into the Sb film. Experience has shown that the evaporation of Sb is a complex process [28]. Its property may have a strong effect on the diffusion process of alkali vapors and eventually the photocathode performance.

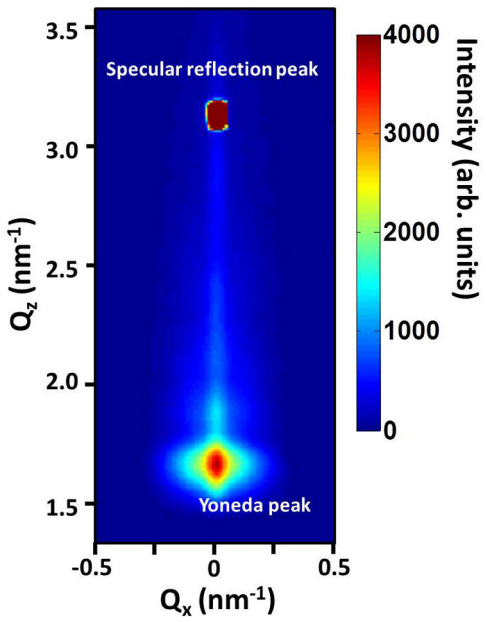

Figure 3. One of the x-ray scattering patterns during Sb evaporation with the specular peak and Yoneda peak labeled.

Figure 3 displays one of the x-ray scattering patterns taken during Sb evaporation at a fixed incidence angle of $\alpha_i = 1.8°$. The specular peak is clearly shown at the position where the exit angle $\alpha_f = \alpha_i$, and the Yoneda peak is observed at the position where the exit angle $\alpha_f = \theta_c$, where θ_c is the film critical angle ($\theta_{c,sb} \sim 0.277°$). Figure 4 shows the specular peak intensity oscillation versus deposition time due to the interference of waves reflected from the top and bottom interfaces [29]. Sb film thickness measured by a pre-calibrated QCM is also plotted. We can see that the oscillation intensity at the beginning of the deposition is relatively low and increases quickly after 40 Å film deposition. The dramatic increase of specular peak intensity indicates a possible film property change around 40 Å, labeled as the transition point in figure 4. From the film growth process point of view [30], the grown antimony forms randomly oriented islands below 40 Å. These islands are smaller than the transverse coherence length of the x-ray used [31][7] to support strong x-ray reflection. At film thickness around 40 Å, these islands coalesce into semi-continuous film with its transverse length larger than the transverse coherence length to support strong x-ray reflection, resulting in the sudden increase of the specular reflection peak intensity. The release of edge and surface energy associated with island coalescence is the strong driving force leading to crystallization [30]. Our previous work on grazing incidence x-ray diffraction (GIXRD) shows that the Sb film on Si transits from amorphous to crystalline structure at a film thickness of 40 Å at the same substrate temperature and growth rate [32], associated with the island coalescence.

[7] The transverse coherence length L_T is calculated to be 300 nm following the equation: $L_T = \frac{\lambda}{2}\left(\frac{R}{D}\right)$, where the wavelength, $\lambda = 1.2$ Å, slit size, $D = 0.2$ mm, and slit to sample distance, $R = 1$ m.

3.2. Growth of the K_2CsSb photocathode

According to the photocathode growth kinetics observed by our previous experiments with crystalline initial antimony films [32], the initial crystalline Sb film is fully dissolved by exposure to alkali vapors prior to forming alkali antimonides. The film that is formed has been shown to be rough, with a roughness similar to the film thickness. The large variation in lattice constant between metallic antimony and potassium antimonides likely leads to the formation of the observed rough surface structure, as the alkali initially diffuses along Sb grain boundaries and pushes the materials apart, forming the observed nano-pillar structure [22]. To prevent this surface roughening, the current photocathode was grown with an initial Sb film thickness less than 40 Å, eliminating the crystalline Sb phase.

A typical photocathode growth process with detailed growth parameters and the film thickness measured by the QCM are summarized in table 1. A 30 Å Sb film, well below the phase transition threshold of 40 Å for the deposition rate used, was first grown on the Si substrate. Exposure of the initial Sb film to K vapor resulted in a photocathode with QE of 0.16% at 532 nm wavelength. Further exposure of the film to Cs vapor resulted in a photocathode with QE of 3.1%. To further enhance the photocathode QE, the process was repeated. A second layer of Sb was deposited with a thickness of 50 Å and the QE dramatically decreased as expected. After exposure of the film to K and Cs, a final QE of 4.9% at 532 nm wavelength was achieved. To ease the following discussion, the film after each deposition will be referred to as $l = 0$, $l = 1$, etc as indicated in table 1. A third layer deposition of Sb and following exposure to K and Cs did not further improve the photocathode QE.

3.3. Specular XRR analysis in photocathode growth

The experimental specular XRR profiles as a function of incident angle θ for samples after each growth step are shown in figure 5. The oscillatory features in specular XRR, i.e. Kiessig fringes, are caused by interference between the x-rays reflected from the film surface and those from the interface of the film and the substrate. The experimental XRR curves were fitted with theoretical curves calculated based on layer structure models following Parratt's recursion method [27], providing information on film thickness, in-plane average electron density, and surface and interface roughness. Since the specular XRR was done after each film growth, several assumptions were made before the XRR fitting. Here, we assumed that (1) the photocathode is a continuous film, (2) the material density across the film is uniform and (3) the initial material density is estimated from the atomic fraction of each element in the chemical formula. The parameter values of film thickness and surface roughness driven from the data via least-squares fitting are reported in table 1. The thickness values obtained from QCM and XRR agree reasonably well for Sb and K deposition. For Cs, a large amount of Cs film is deposited according to the QCM measurement, but the XRR shows only a modest increase of total film thickness.

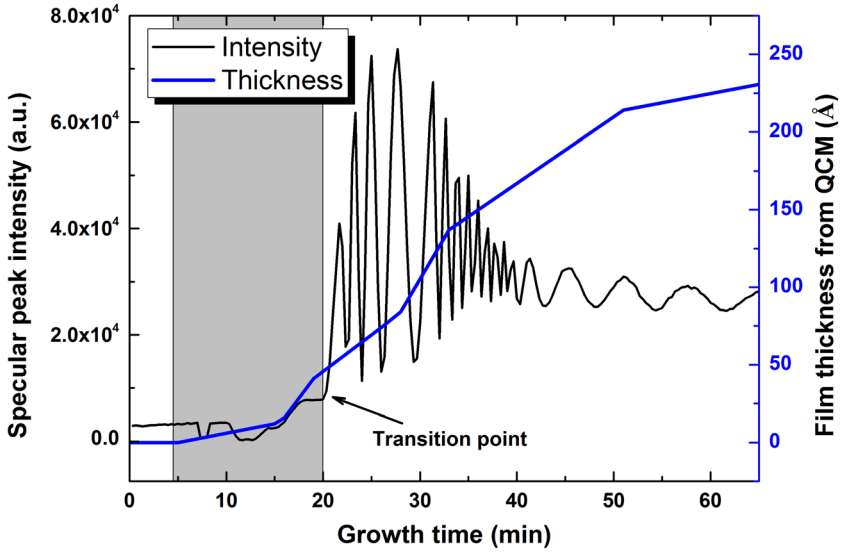

Figure 4. Specular peak intensity oscillation and QCM measured Sb film thickness as a function of growth time.

Table 1. Growth conditions for the photocathode and optimal parameter values obtained from least-square fitting of XRR data.

Layer ID	Recipe	Deposited film thickness (QCM)	QE after deposition	Total film thickness (XRR)	Roughness (XRR)
$l = 6$	Cs–K–Sb–Cs–K–Sb/Si	440 Å	4.9%	469 Å	32.0 Å
$l = 5$	K–Sb–Cs–K–Sb/Si	160 Å	0.88%	449 Å	36.0 Å
$l = 4$	Sb–Cs–K–Sb/Si	50 Å	—	200 Å	21.3 Å
$l = 3$	Cs–K–Sb/Si	420 Å	3.1%	174 Å	13.2 Å
$l = 2$	K–Sb/Si	120 Å	0.16%	141 Å	10.5 Å
$l = 1$	Sb/Si	30 Å	—	35 Å	2.9 Å
$l = 0$	Si substrate	—	—	—	3.1 Å

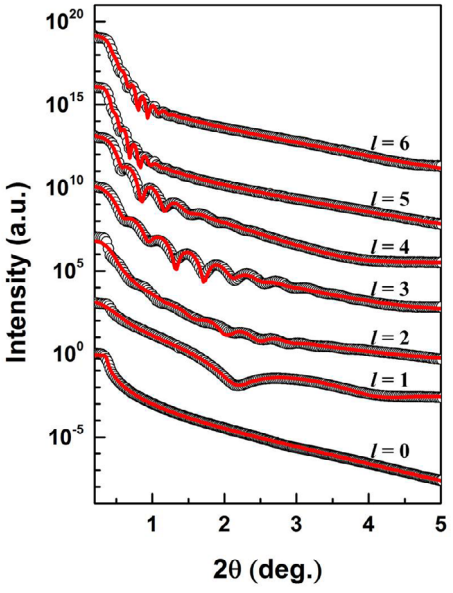

Figure 5. Experimental data (points) and simulation (solid line) of XRR profiles after each growth step. The plots are offset for clarity. The well-defined Kiessig fringes in the XRR curves represent uniform films after each growth step, the oscillation decay rate increases as the growth process proceeds, indicating that the film roughness becomes larger.

This difference is most likely due to the fact that the QCM was water cooled at 15 °C, while the film growth sample was heated at 125 °C. Since Cs has a low melting point of 28 °C [33], the Cs atoms deposited on the sample at 125 °C have a much faster evaporation rate than those deposited on the water cooled QCM. The quick loss of cesium atoms in K_2CsSb and Cs_3Sb photocathodes due to evaporation over 50 °C was also reported previously [34]. As in a dynamic vacuum system, extra Cs atoms which evaporated from the photocathode surface were pumped out through the vacuum pump system.

The well-defined Kiessig fringes in the XRR curves represent uniform density films after each growth step [35]. Most likely, the Sb and alkali antimonide films have high defect concentrations, such as grain boundaries and subsequently deposited atoms can easily diffuse into the film to form compounds. This diffusion is a fast process at 125 °C, resulting in uniform density films after each deposition. The theoretical fit of the XRR profiles reveals that the film thickness increases to about four times the initial Sb thickness after K exposure and further increases to about five times the initial Sb thickness after Cs exposure. This agrees with the empirical diagram in section 2.1. The exposure of the Sb film to K vapor is a redox-reaction which forms K–Sb compounds, mainly K_3Sb as can be seen from figure 8. During the interaction of Cs vapor with the K_xSb phase, the Cs atoms, with a larger

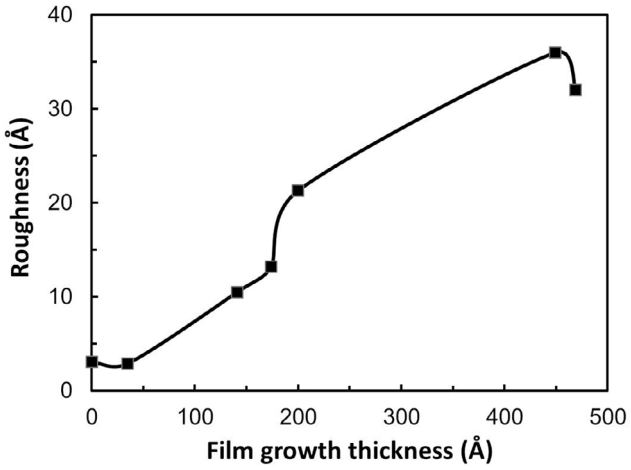

Figure 6. Film roughness versus film thickness. Note the sharp increase observed in sample $l = 4$ and a slightly reduced roughness in sample $l = 6$.

ionic radius than that of K atom, replace K atoms in the cubic K_3Sb structure to form K_2CsSb, further increasing the film thickness. The film thickness evolution is further investigated by separating the entire photocathode growth process into two similar process cycles, $l = 1$–3 and $l = 4$–6. Since the Sb diffuses into the K_2CsSb film in step $l = 4$, the diffused Sb thickness cannot be directly calculated from the XRR result and a relative comparison is done here. In process cycle $l = 1$–3, with a 30 Å (QCM) initial Sb film on silicon, the K_2CsSb film thickness is 174 Å (XRR). In process cycle $l = 4$–6, with a 50 Å (QCM) diffused Sb film, the increase of K_2CsSb film thickness is 295 Å (=469 Å–174 Å) and is proportional to a K_2CsSb film thickness with a 50 Å initial Sb film. This result indicates that the K_2CsSb film thickness is determined by the Sb film thickness regardless of how the Sb film was grown. This may provide an indirect method to estimate the thickness of a K_2CsSb photocathode grown in a setup without XRR, i.e. by monitoring the total Sb thickness via QCM.

The rapid damping of the interference fringes observed in the XRR profile at higher angles is closely related to the film surface roughness normal to the interface. The larger the roughness of a film, the faster the oscillation decay rate of XRR. As shown in figure 5, for the silicon substrate before film growth, no oscillation was observed since there is no electron density difference. A theoretical fitting of Si gives surface roughness of $\sigma = 3.1$ Å, confirming its atomic flat surface morphology. After the deposition of thin films, the oscillation can be observed and the oscillation decay rate increases as the growth process proceeds, indicating the film roughness becomes larger. Theoretical fitting of the result shows an increase of the surface roughness from $\sigma = 3.1$ Å to $\sigma = 32$ Å as the growth process proceeds and a sharp increase of the surface roughness in sample $l = 4$ with respect to the increase of film thickness (figure 6). The roughness evolution in photocathode growth reveals that the surface roughening process mainly happens during the exposure to K vapor; the K atoms diffuse and penetrate into the Sb film lattice to form a K_3Sb structure with increased film thickness, resulting in a rough surface morphology possibly initiated by lattice expansion on

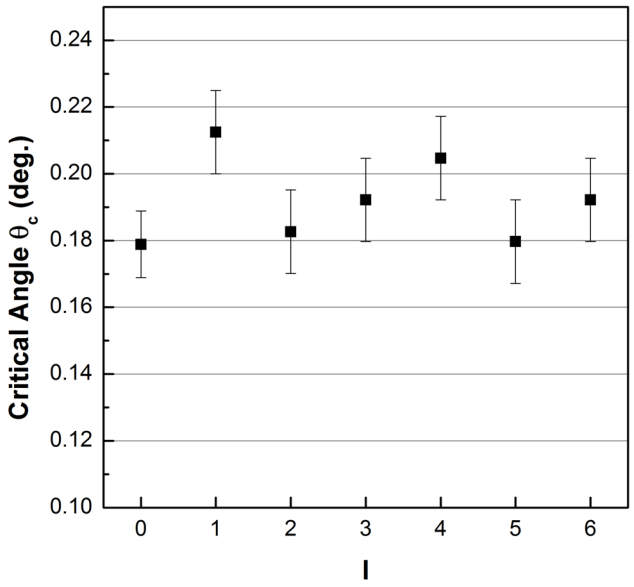

Figure 7. Positions of the critical angle for each films $l = 0$–6 as defined in table 1.

formation of the antimonide. The sharp roughness increase in sample $l = 4$ is possibly due to a 'harder' process of Sb penetrating into the crystalline K_2CsSb lattice than that of K or Cs penetration. A slightly reduced roughness in sample $l = 6$ is due to a better crystallinity of the photocathode film at the end. We must emphasize here that the final photocathode film grown through the multi-step process exhibits a surface roughness of ~3 nm, which is an order of magnitude lower than the reported value (~25 nm [22]) of a conventionally made photocathode film from crystalline Sb for the same overall thickness.

The critical angle (θ_c) for total external reflection is an important parameter from XRR measurement. It is determined by the surface film electron density (ρ in $Å^{-3}$): the greater the film electron density, the larger the critical angle. The surface film electron density can be extracted from the following equation [36]:

$$\theta_c^2 = 2\delta = \frac{r_e \lambda^2}{\pi}\rho \qquad (2)$$

where δ is the dispersive correction to the index of refraction for x-rays, usually in the order of 10^{-5}, $r_e = 2.82 \times 10^{-6}$ nm is the classical radius of an electron, λ is the x-ray wavelength and ρ is the surface film electron density. The film mass density d_m (in g cm^{-3}) can also be extracted with known stoichiometric composition. We determined the critical angle positions analytically using Parratt's approximation that the critical angle is that angle at which the reflected intensity is half the totally reflected intensity [27]. Figure 7 shows the critical angle positions for films $l = 0$–6 as defined in table 1. A critical angle of $\theta_c \sim 0.277°$ is expected for a uniform crystalline Sb film, higher than the observed critical angle $\theta_c \sim 0.213°$ exhibited by sample $l = 1$. A smaller observed critical angle position indicates a lower density, corresponding to an expected amorphous Sb film. The exposure to K vapor forms a film with lower average density, and the exposure to Cs vapor forms a film with slightly higher average density.

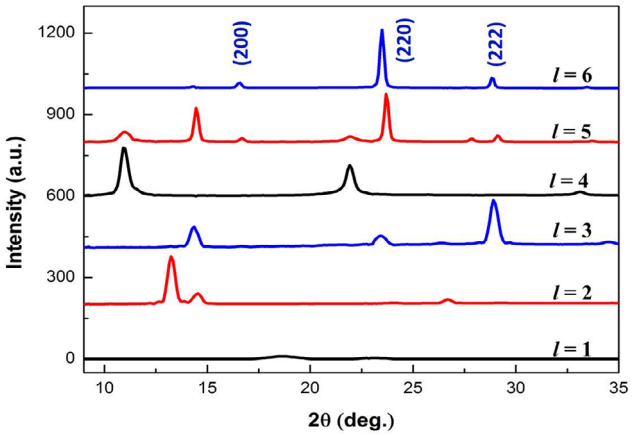

Figure 8. Crystalline evolution of the photocathode during growth, observed via XRD. The plots are offset for clarity.

3.4. XRD analysis in photocathode growth

XRD measurements from $2\theta = 9°$ to $2\theta = 35°$ were taken for films $l = 1$–6 to elucidate the evolution of atomic structure (figure 8). The XRD patterns are compared individually with the international centre for diffraction data (ICDD) powder files to identify film structures. The XRD pattern shows very weak and broad diffraction peaks for the initial Sb deposition, expected for an amorphous film. The presence of amorphous Sb is consistent with the low density observed by XRR. The first exposure of the Sb film to K vapor results in a mixed phase of cubic and hexagonal potassium antimonides, and the exposure to Cs vapor results in K_2CsSb formation. With the second Sb deposition, there is no evidence of Sb and K_2CsSb crystalline structures. Further exposure to K yields cubic K_3Sb and a small amount of KSb. The final exposure to Cs transforms the photocathode fully to K_2CsSb.

4. Conclusion

In conclusion, a low roughness, high QE K_2CsSb photocathode was grown by alternately introducing Sb, K and Cs vapors. A particular feature of this work is that the initial thickness of Sb was less than the critical thickness of amorphous to crystalline phase transition. The photocathode obtained through the multi-step process exhibits a significantly smoother surface compared to a conventionally made film from crystalline Sb for the same overall thickness. The growth process was systematically studied via synchrotron x-ray methods including GISAXS, XRR and XRD. GISAXS data show a transition point of the Sb film on Si at a film thickness of 40 Å. XRR and XRD patterns of films after each growth step reveal the evolution of film thickness, roughness, electron density and structure during the photocathode growth. Further investigation indicates that the K_2CsSb photocathode thickness is around five times that of the total deposited Sb film regardless of how the Sb film was grown. A bulk diffusion process increases the film surface morphology mainly during the K diffusion process. The film surface roughening process happens first at the step when K diffuses into the Sb crystalline. XRD measurements show that the material goes through two structural changes of the crystalline phase during formation, from crystalline Sb to K_3Sb and finally to K_2CsSb.

Acknowledgments

The authors thank Zhang Jiang, physicist at Argonne National Laboratory, for his help and discussion on XRR analysis, as well as Arthur Woll, Sr Research Associate at Cornell University, for his help on XRR measurement and discussion. Work at Argonne National Laboratory was supported by the U S Department of Energy, Office of Science, Office of Basic Energy Sciences and Office of High Energy Physics under contract DE-AC02-06CH11357. Work at BNL, LBNL and Stony Brook University was supported by the US DOE, under contracts DE-AC02-05CH11231, DE-AC02-98CH10886, KC0407-ALSJNT-I0013, and DE-SC0005713. Use of the National Synchrotron Light Source, Brookhaven National Laboratory, was supported by the U S Department of Energy, Office of Science, Office of Basic Energy Sciences, under Contract No. DE-AC02-98CH10886. Use of CHESS was supported by the NSF & NIH/NIGMS via NSF award DMR-1332208.

References

[1] Kong S H, Kinross-Wright J, Nguyen D C and Sheffield R L 1995 *Nucl. Instrum. Methods Phys. Res.* A **358** 272
[2] Yang J, Sakai F, Yanagida T, Yorozu M, Okada Y, Takasago K, Endo A, Yada A and Washio M 2002 *J. Appl. Phys.* **92** 1608
[3] Wang X J, Rao T S, Batchelor K, Ben-Zvi I and Fischer J 1995 *Nucl. Instrum. Methods Phys. Res.* A **356** 159
[4] Moszynski M, Gierlik M, Kapusta M, Nassalski A, Szczesniak T, Fontaine Ch and Lavoute P 2006 *Nucl. Instrum. Methods Phys. Res.* A **567** 31
[5] Kume H, Suzuki S, Takeuchi J and Oba K 1985 *IEEE Trans. Nucl. Sci.* **32** 448
[6] Spicer W E 1977 *Appl. Phys.* **12** 115
[7] Child C D 1911 *Phys. Rev.* **32** 492
[8] Vecchione T, Feng J, Wan W, Padmore H A, Ben-Zvi I, Liang X, Ruiz-Oses M, Rao T, Smedley J and Dowell D 2012 *Proc. 2012 Int. Accelerator Conf.* p 655
[9] Dowell D H, Bazarov I, Dunham B, Harkay K, Hernandez-Garcia C, Legg R, Padmore H, Rao T, Smedley J and Wan W 2010 *Nucl. Instrum. Methods Phys. Res.* A **622** 685
[10] Rao T *et al* 2006 *Nucl. Instrum. Methods Phys. Res.* A **557** 124
[11] van Oerle B M and Ernst G J 1995 *Nucl. Instrum. Methods Phys. Res.* A **358** 287
[12] Bazarov I V, Cultrera L, Bartnik A, Dunham B, Karkare S, Li Y, Xianghong X, Maxson J and Roussel W 2011 *Appl. Phys. Lett.* **98** 224101
[13] Cultrera L, Karkare S, Lillard B, Bartnik A, Bazarov I, Dunham B, Schaff W and Smolenski K 2013 *Appl. Phys. Lett.* **103** 103504
[14] Vecchione T, Ben-Zvi I, Dowell D H, Feng J, Rao T, Smedley J, Wan W and Padmore H A 2011 *Appl. Phys. Lett.* **99** 034103
[15] Cultrera L, Bazarov I, Bartnik A, Dunham B, Karkare S, Merluzzi R and Nichols M 2011 *Appl. Phys. Lett.* **99** 152110
[16] Sommer A H 1963 *Appl. Phys. Lett.* **3** 62
[17] Nathan R and Mee C H B 1967 *Int. J. Electron.* **23** 349

[18] McCarroll W H 1965 *J. Phys. Chem. Solids* **26** 191
[19] Ettema A R H F and de Groot R A 2002 *Phys. Rev.* B **66** 115102
[20] Kapusta M, Lavoute P, Lherbet F, Rossignol E, Moussant C and Fouche F 2007 *Proc. 2007 IEEE Nuclear Science Symp. Conf. Record* vol 1 p 73
[21] Nakamura K, Hamana Y, Ishigami Y and Matsui T 2010 *Nucl. Instrum. Methods Phys. Res.* A **623** 276
[22] Schubert S *et al* 2013 *APL Mater.* **1** 032119
[23] Renaud G *et al* 2003 *Science* **300** 1416
[24] Chason E and Mayer T M 1997 *Crit. Rev. Solid State Mater. Sci.* **22** 1
[25] Suryanarayana C and Norton M G 1998 *X-ray Diffraction: a Practical Approach* (New York: Plenum)
[26] Sommer A H 1966 *J. Appl. Phys.* **37** 2789
[27] Parratt L G 1954 *Phys. Rev.* **95** 359
[28] Sommer A H 1968 *Photoemissive Materials: Preparation, Properties and Uses* (New York: Wiley)
[29] Wang Y, Zhou H, Zhou L, Headrick R L, Macrander A T and Ozcan A S 2007 *J. Appl. Phys.* **101** 023503
[30] Petrov I, Bama P B, Hultman L and Greene J E 2003 *J. Vac. Sci. Technol.* A **21** S117
[31] Als-Nielsen J and McMorrow D 2011 *Elements of Morden X-Ray Physics* 2nd edn (New York: Wiley)
[32] Ruiz-Oses M *et al* 2014 *APL Mater.* **2** 121101
[33] Haynes W M 2014 *CRC Handbook of Chemistry and Physics* 95th edn (Boca Raton, FL: CRC Press)
[34] Montgomery E J, Feldman D W, O'Shea P G, Pan Z, Moody N A and Jensen K L 2007 *IEEE Nucl. Sci. Symp. Conf. Record* vol C070625 p 2016
[35] Dourdain S, Bardeau J, Colas M, Smarsly B, Mehdi A, Ocko B M and Gibaud A 2005 *Appl. Phys. Lett.* **86** 113108
[36] Pietsch U, Holy V and Baumbach T 2004 *High-Resolution X-ray Scattering* 2nd edn (Berlin: Springer)